

A Study of Steady Buoyancy-Driven Dissipative Micropolar Free Convection Heat and Mass Transfer in a Darcian Porous Regime with Chemical Reaction

O. Anwar Bég¹, R. Bhargava², S. Rawat², H. S. Takhar³, Tasweer A. Bég⁴

¹Fire Safety Engineering Program, Leeds College of Building
North Street, Leeds, LS2 7QT, England, UK
obeg@lcb.ac.uk

²Department of Mathematics, Indian Institute of Technology
Roorkee, India
rbharfma@iitr.ernet.in

³Engineering Department, Manchester Metropolitan University
Oxford Rd., Manchester, M5 1GD, UK
h.s.takhar@mmu.ac.uk

⁴Engineering Mechanics Research, 18 Milton Grove
Manchester, M16 0BP, UK
ihd001@hotmail.com

Received: 15.06.2006 **Revised:** 12.10.2006 **Published online:** 05.05.2007

Abstract. In the present paper we examine the steady double-diffusive free convective heat and mass transfer of a chemically-reacting micropolar fluid flowing through a Darcian porous regime adjacent to a vertical stretching plane. Viscous dissipation effects are included in the energy equation. Assuming incompressible, micro-isotropic fluid behaviour the transport equations are formulated in a two-dimensional coordinate system (x, y) using boundary-layer theory. The influence of the bulk porous medium retardation is modeled as a drag force term in the translational momentum equation. Transformations render the conservation equations into dimensionless form in terms of a single independent variable, η , transverse to the stretching surface. A simplified first order homogenous reaction model is also used to simulate chemical reaction in the flow. Using the finite element method solutions are generated for the angular velocity field, translational velocity field, temperature and species transfer fields. The effects of buoyancy, porous drag and chemical reaction rate are studied. Chemical reaction is shown to decelerate the flow and also micro-rotation values, in particular near the wall. Mass transfer is also decreased with increasing chemical reaction rate. Increasing Darcy number is shown to accelerate the flow. Applications of the study include cooling of electronic circuits, packed-bed chemical reactors and also the near field flows in radioactive waste geo-repositories.

Keywords: micropolar, reactive flow, heat and mass transfer, porous media, numerical, buoyancy, viscous dissipation, finite elements.

1 Introduction

Micropolar convection flows have been analyzed by many authors following the seminal work of Eringen who introduced the micropolar fluid [1] as a special case of the micromorphic fluid [2]. Such fluids can accurately simulate the micro-rotational effects observed in colloidal solutions, blood, dielectric fluids, plasmas, liquid crystals etc. Micropolar convective flows find applications in the purification of crude oil, polymer technologies, centrifugal separation processes, cooling tower dynamics, chemical reaction engineering, metallurgical drawing of filaments and solar energy systems. Bhargava et al. [3] studied the combined free and forced convection of a micropolar fluid past a stretching surface with applications in polymer processing. Chamkha et al. [4] presented an interesting study of the combined micropolar heat transfer and flow in a vertical channel. Such studies were confined to purely fluid regimes. Porous media however constitute a growing importance in many manufacturing and environmental systems. These include grain storage systems, heat pipes, packed microsphere insulation, distillation towers, ion exchange columns, subterranean chemical waste migration, solar power absorbers etc. Many studies of both Newtonian and non-Newtonian heat transfer in porous media have been presented. Kaviany [5] also provides an excellent treatment of applications of convection as well as conduction and radiative heat transfer in porous media. Recent studies include those by Chamkha [6] who discussed the unsteady flow of an Ostwald-deWaele pseudoplastic fluid in a Darcian porous medium. More recently Bég et al. [7] studied the influence of Rossby number and thermal stratification on rotating convection in a non-Darcian porous medium. Micropolar flow and transport in porous media has received less attention despite important applications in emulsion filtration, polymer gel dynamics in packed beds, petroleum and lubrication flows in porous wafers. Several studies have however been communicated both with and without heat transfer. Aganovic and Tutek [8] examined the dynamics of a micropolar creeping flow through a Darcian porous medium using the homogenization method. The free convective boundary layer flow through a Darcian porous medium was studied using a shooting method by Mohammedin et al. [9]. Elbarbary and Elgazery [10] considered the hydromagnetic convection in a porous regime using the Chebyshev finite difference method also reporting on the influence of thermal radiative flux and variable viscosity on the micro-rotation and temperature profiles. An excellent study of two-dimensional coupled magneto-convective heat and mass transfer in micropolar flow through a Darcian porous medium was communicated by Kim [11] who also obtained solutions using the Keller-box implicit method. Chamkha et al. [12] studied the combined heat and mass transfer of a chemically-reacting micropolar fluid in a porous medium. More recently Bhargava et al. [13] have studied convective heat and mass transfer of a micropolar fluid in a Darcian porous square cavity with heat source effects using finite element and finite difference methods. These studies did not consider the important effect of viscous mechanical dissipation. Such effects can be important in geophysical flows and also certain industrial operations and are usually characterized by the Eckert number. A number of authors have considered viscous heating effects on Newtonian convection flows. Rajasekaran and Palekar [14] studied the influence of Eckert number on rotating mixed convection using Merk's series expansions. For the

case of uniform wall temperature, increasing the Eckert number reduces heat transfer rates. However for an equivalent viscous dissipation effect, heating by uniform heat flux produced larger Nusselt number compared with the uniform wall temperature case. Mahajan and Gebhart [15] reported on the influence of viscous heating dissipation effects in natural convection flows, showing that heat transfer rates are depressed by an increase in the dissipation parameter. Bég et al. [16] studied the influence of vorticity diffusion and viscous dissipation on thermoconvection flow in a non-Darcian porous medium. Koo and Kleinstreuer [17] considered the influence of viscous heating on microtube and microchannel convection regimes. Haddad et al. [18] considered the influence of viscous heating on entropy generation due to laminar incompressible forced convection flow through a parallel-plate microchannel configuration. These studies of viscous heating effects have been confined to Newtonian flows. The present study considers such an effect in micropolar fluids. A limited number of studies have considered viscous dissipation effects in micropolar thermal convection. Soundalgekar and Takhar [19] have provided one of the earliest studies of viscous dissipation effects on micropolar heat transfer past a wedge. A rise in Ec from 0.01 to 0.02 was shown to induce a decrease in the heat transfer rate at the wedge surface. Mansour and Gorla [20] more recently presented a boundary layer solution for transient free micropolar convection heat transfer with Joule thermoelectric effects. Viscous dissipation was shown numerically to decrease heat transfer rates. An excellent analysis of micropolar stagnation thermal boundary layer flow on a moving surface was presented by Bhargava and Takhar [21] for both non-dissipative and dissipative cases.

In the present analysis we shall consider the viscous dissipation and buoyancy effects on micropolar chemically-reactive convective heat and mass transfer past a stretching surface adjacent to a micropolar fluid-saturated porous medium. Such a study goes beyond those already reported and constitutes an important addition to the scientific literature on environmental contamination, geophysical transport phenomena and also reactive non-Newtonian thermofluid dynamics in the process industries.

2 Dynamics of thermo-micropolar fluids

In this study the thermo-micropolar non-Newtonian fluid model is implemented. Such a fluid is a special sub-class of the much more complex micromorphic fluid. In thermo-micropolar fluid mechanics, the classical continuum and thermodynamics laws are extended with additional equations which account for the conservation of micro-inertia moments and the balance of first stress moments which arise due to the consideration of micro-structure in a fluid. Hence new kinematic variables (gyration tensor, microinertia moment tensor), and concepts of body moments, stress moments and microstress are combined with classical continuum fluid dynamics theory. Thermo-micropolar fluids can accurately simulate liquids consisting of randomly orientated particles suspended in a viscous medium and offer an excellent framework to study advanced geophysical and environmental pollution flows. The governing equations for thermo-micropolar fluids in terms of vector fields may be presented following Eringen [22] and Lukaszewicz [23], as

follows:

conservation of mass:

$$\frac{\partial \rho}{\partial t} = -\rho \nabla \cdot \underline{V}; \quad (1)$$

conservation of translational momentum:

$$\frac{\partial \underline{V}}{\partial t} = -\nabla p + \kappa \nabla \times \underline{\omega}^* - (\mu + \kappa) \nabla \times \nabla \times \underline{V} + (\lambda_e + 2\mu + \kappa) \nabla \nabla \cdot \underline{V} + \rho \underline{f}_b; \quad (2)$$

conservation of angular momentum (micro-rotation):

$$\rho j^* \frac{\partial \underline{\Omega}}{\partial t} = \kappa \nabla \times \underline{V} - 2\kappa \underline{\omega}^* - \gamma \nabla \times \nabla \times \underline{\omega}^* + (\alpha_v + \beta_v + \gamma) \nabla (\nabla \cdot \underline{\omega}^*) + \rho \underline{l}; \quad (3)$$

conservation of energy (heat):

$$\rho \frac{\partial E}{\partial t} = -p \nabla \cdot \underline{V} + \rho \Phi - \nabla \cdot \underline{q}; \quad (4)$$

dissipation function of mechanical energy per unit mass:

$$\begin{aligned} \rho \Phi = & \lambda_e (\nabla \cdot \underline{V})^2 + 2\mu D_T : D_T + 4\kappa \left(\frac{\nabla}{2} \times \underline{V} - \underline{\omega}^* \right)^2 \\ & + \alpha_v (\nabla \cdot \underline{\omega}^*)^2 + \gamma \nabla \underline{\omega}^* : \nabla \underline{\omega}^* + \beta_v \nabla \underline{\omega}^* : (\nabla \underline{\omega}^*)^T; \end{aligned} \quad (5)$$

deformation tensor:

$$D_T = \frac{1}{2} [\underline{V}_{ij} + \underline{V}_{ji}], \quad (6)$$

where E is the specific internal energy, q the heat flux, Φ is the viscous dissipation function of mechanical energy per unit mass, ρ denotes the mass density of thermo-micropolar fluid, \underline{V} is translational velocity vector, $\underline{\omega}^*$ is angular velocity (microrotation or gyration) vector, j^* is microinertia, p is the thermodynamic pressure, \underline{f}_b is the body force per unit mass vector, \underline{l} is the body couple per unit mass vector, μ is the Newtonian dynamic viscosity, λ_e is the Eringen second order viscosity coefficient, κ is the vortex (microrotation) viscosity coefficient, and α_v, β_v and γ are spin gradient viscosity coefficients for thermo-micropolar fluids. In the special case where the fluid has constant physical properties, no external body forces exist and for steady state flow, the conservation equations can be greatly simplified. Additionally for the case where $\kappa = \alpha = \beta = \gamma = 0$ and with vanishing \underline{l} and \underline{f}_b , the gyration vector disappears and equation (3) due to Eringen [22] vanishes. Equation (2) also reduces in this special case to the classical Navier-Stokes equations. We also note that for the case of zero vortex viscosity (κ) only, the velocity vector \underline{V} and the micro-rotation vector $\underline{\omega}^*$ are decoupled and the global motion is unaffected by the micro-rotations. A simplified version of these equations is utilized in the mathematical transport model presented next.

3 Mathematical model

We examine the laminar boundary layer heat and mass transfer of a micropolar chemically-reacting fluid against gravity past a vertical stretching surface adjacent to a Darcian micropolar-fluid-saturated porous medium. Concentration of species in the free stream i.e. far away from the stretching surface, is assumed to be infinitesimal (zero) and defined as C_∞ . Temperature in the free stream is taken as T_∞ . The x -axis is located parallel to the vertical surface and the y -axis normal to it. Constant micropolar fluid properties are assumed throughout the medium i.e. density, mass diffusivity, viscosity and chemical reaction rate are fixed. In the general Navier-Stokes equations, the Rayleigh expression for viscous dissipation due to internal friction in the fluid per unit volume, takes the form:

$$\begin{aligned} & \frac{2}{3}\mu \left[\left(\frac{\partial v}{\partial y} - \frac{\partial w}{\partial z} \right)^2 + \left(\frac{\partial w}{\partial z} - \frac{\partial u}{\partial x} \right)^2 + \left(\frac{\partial u}{\partial x} - \frac{\partial v}{\partial y} \right)^2 \right] \\ & + \mu \left[\left(\frac{\partial w}{\partial y} + \frac{\partial v}{\partial z} \right)^2 + \left(\frac{\partial u}{\partial z} + \frac{\partial w}{\partial x} \right)^2 + \left(\frac{\partial v}{\partial x} + \frac{\partial u}{\partial y} \right)^2 \right]. \end{aligned} \quad (7)$$

For boundary layer flows the y -direction velocity gradient i.e.

$$\left(\frac{\partial u}{\partial y} \right) \gg \frac{\partial u}{\partial x}, \frac{\partial u}{\partial z}, \frac{\partial v}{\partial x}, \frac{\partial v}{\partial y}, \frac{\partial v}{\partial z}, \frac{\partial w}{\partial x}, \frac{\partial w}{\partial y}, \frac{\partial w}{\partial z}.$$

Therefore we only retain, following Schlichting [24] the $\left(\frac{\partial u}{\partial y} \right)^2$ component in the general three-dimensional viscous dissipation term. Chemical reaction of the micropolar fluid is assumed to be homogenous and first order. The governing transport equations for the flow regime, illustrated in Fig. 1, incorporating a linear Darcian drag can be shown to take the

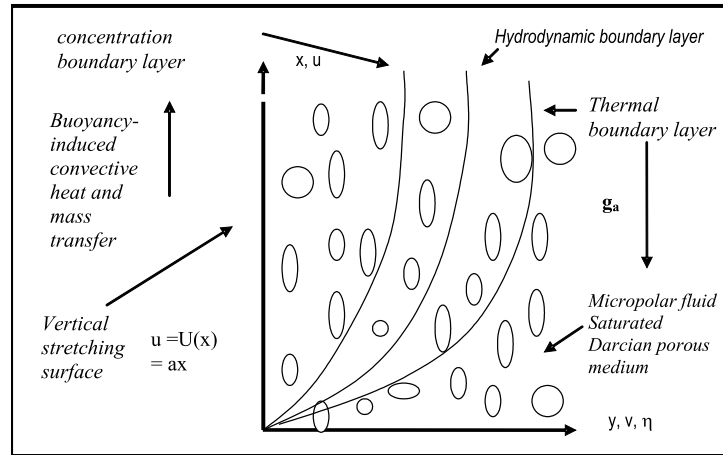


Fig. 1. Geometry of flow regime.

following form, under these approximations and in consistency with the Boussinesq and boundary-layer approximations:

conservation of mass:

$$u \frac{\partial u}{\partial x} + v \frac{\partial v}{\partial y} = 0; \quad (8)$$

conservation of linear momentum:

$$u \frac{\partial u}{\partial x} + v \frac{\partial u}{\partial y} = \nu \frac{\partial^2 u}{\partial y^2} + k_1 \frac{\partial N}{\partial y} - \frac{\nu}{k_p} u + \beta g_a (T - T_\infty) + \beta^* g_a (C - C_\infty); \quad (9)$$

conservation of angular momentum:

$$u \frac{\partial N}{\partial x} + v \frac{\partial N}{\partial y} = \frac{\gamma}{\rho j^*} \frac{\partial^2 N}{\partial y^2} - \frac{\kappa}{\rho j^*} \left[2N + \frac{\partial u}{\partial y} \right]; \quad (10)$$

conservation of micro-inertia:

$$u \frac{\partial j^*}{\partial x} + v \frac{\partial j^*}{\partial y} = 0; \quad (11)$$

conservation of energy:

$$u \frac{\partial T}{\partial x} + v \frac{\partial T}{\partial y} = \alpha \frac{\partial^2 T}{\partial y^2} + \frac{\nu}{c_p} \left(\frac{\partial u}{\partial y} \right)^2; \quad (12)$$

conservation of species diffusion:

$$u \frac{\partial C}{\partial x} + v \frac{\partial C}{\partial y} = D \frac{\partial^2 C}{\partial y^2} - \Gamma C. \quad (13)$$

In equation (9) the porous matrix resistance at low Reynolds numbers i.e. the Darcian bulk impedance is defined by the term $-\frac{\nu}{k_p} u$. The boundary conditions on the vertical surface and far away from the surface (in the free stream) can be defined as follows:

$$y = 0: \quad u = U(x), \quad v = 0, \quad T = T_w, \quad C = C_w, \quad N = -s \left[\frac{\partial u}{\partial y} \right], \quad (14)$$

$$y \rightarrow \infty: \quad u = 0, \quad T = T_\infty, \quad C = C_\infty, \quad N \rightarrow 0, \quad (15)$$

where $\nu = \frac{\mu + \kappa}{\rho}$ denotes the apparent kinematic viscosity, $k_1 = \frac{\kappa}{\rho}$ ($k_1 > 0$) is the Eringen micropolar coupling constant, s is the surface condition parameter and varies from 0 to 1 and $U(x)$ is the surface velocity of the stretching wall. In equations (8) through (13), u and v are the x -direction (streamwise) and y -direction (spanwise) fluid velocities, g_a denotes gravitational acceleration, j^* is micro-inertia per unit mass, κ is micropolar vortex viscosity, γ is the micropolar spin gradient viscosity, C designates species concentration

in the boundary layer, C_∞ is the concentration at the free stream, T_w is concentration at the wall, C_w is concentration at the wall (stretching surface), β is the coefficient of volume expansion, T is temperature, N is the angular velocity (micro-rotation), ν denotes kinematic viscosity, k_p is permeability of the porous medium, α is the thermal diffusivity, D is the species diffusivity and Γ is the chemical reaction rate parameter. Subscripts $()_w$ and $()_\infty$ denote conditions at the wall and free stream respectively. In (14) the initial boundary condition for micro-rotation physically corresponds to the *vanishing of the anti-symmetric part of the stress tensor* and corresponds to *weak* concentrations of the micro-elements of the thermo-micropolar fluid. The microelement (particle) spin is equal to the fluid vorticity at the boundary for fine particle suspensions. In this scenario therefore the particles are able to sustain rotation in the vicinity of the stretching surface (near-field regime). At the wall, the normal component of the translational velocity, v , is zero due to the absence of transpiration effects i.e. there is no lateral mass flux. The continuity (mass conservation) equation is automatically satisfied by defining a stream function using the Cauchy-Riemann equations, $\psi(x, y)$ such that:

$$u = \frac{\partial \psi}{\partial y}, \quad (16)$$

$$v = -\frac{\partial \psi}{\partial x}. \quad (17)$$

Proceeding with the analysis, we now define the following transformations to reduce the mathematical model into dimensionless form:

$$\psi = [\nu x U(x)]^{1/2} f(\eta), \quad (18)$$

$$\eta = \left[\frac{U(x)}{\nu x} \right]^{1/2} y, \quad (19)$$

$$N = \sqrt{\frac{U(x)}{\nu x}} U(x) g(\eta), \quad (20)$$

$$U(x) = ax, \quad (21)$$

$$\lambda = \frac{\gamma}{\rho j^* \nu}, \quad (22)$$

$$G^* = \frac{\gamma U(x)}{\kappa \nu x}, \quad (23)$$

$$h = \frac{T - T_\infty}{T_w - T_\infty}, \quad (24)$$

$$j = \frac{C - C_\infty}{C_w - C_\infty}, \quad (25)$$

where η is dimensionless transverse (spanwise) coordinate, f is dimensionless stream function, g is dimensionless micro-rotation function, h is dimensionless temperature function, j is dimensionless concentration, λ and G^* are micropolar material parameters and a denotes a dimensional constant ($a > 0$). Introducing these non-dimensional transformations reduces the conservations equations from an (x, y) coordinate system

to an (η) coordinate system, with the continuity equation identically satisfied by the Cauchy-Riemann equations (16) and (17) leading to the following coupled set of non-linear ordinary differential equations in terms of the four dependent variables f, g, h, j and the new independent variable, η .

Conservation of momentum:

$$\frac{d^3 f}{d\eta^3} + B_1 \frac{dg}{d\eta} + f \frac{d^2 f}{d\eta^2} - \left(\frac{df}{d\eta} \right)^2 + Gr_x Re_x h + Gm_x Re_x j - \frac{1}{Re_x Da_x} \frac{df}{d\eta} = 0; \quad (26)$$

conservation of angular momentum:

$$\lambda \frac{d^2 g}{d\eta^2} - \frac{\lambda}{G^*} \left(2g + \frac{d^2 f}{d\eta^2} \right) - \frac{df}{d\eta} g + f \frac{dg}{d\eta} = 0; \quad (27)$$

conservation of energy:

$$\frac{d^2 h}{d\eta^2} + Pr f \frac{dh}{d\eta} + Pr Ec \left(\frac{d^2 f}{d\eta^2} \right)^2 = 0; \quad (28)$$

conservation of species:

$$\frac{d^2 j}{d\eta^2} + Sc f \frac{dj}{d\eta} - Sc \left[\chi Re_x j + j \frac{df}{d\eta} \right] = 0, \quad (29)$$

where $Re_x = \frac{Ux}{\nu}$ is the local Reynolds number, $Gr_x = \frac{\nu g_a \beta [T_w - T_\infty]}{U^3}$ is the local Grashof number (buoyancy parameter for free thermo-convective heat transfer), $Gm_x = \frac{\nu g_a \beta^* [C_w - C_\infty]}{U^3}$ is the species Grashof (free convective mass transfer i.e. buoyancy) parameter, $Da_x = \frac{k_p}{x^2}$ is the local Darcy number, $Ec = \frac{U^2}{C_p (T_w - T_\infty)}$ is the Eckert viscous dissipation number, $Sc = \frac{\nu}{D}$ is the Schmidt number, $Pr = \frac{\nu}{\alpha}$ is the Prandtl number, $\chi = \frac{\nu \Gamma}{U^2}$ is dimensionless chemical reaction rate parameter and $B_1 = \frac{k_1}{\nu} = \frac{\kappa}{\mu}$ is the micropolar coupling parameter. The corresponding transformed boundary conditions for the problem now become:

initial:

$$\eta = 0: \quad f(0) = 0, \quad \frac{df}{d\eta}(0) = 1, \quad h(0) = 1, \quad j(0) = 1, \quad g(0) = -s \frac{d^2 f}{d\eta^2}(0); \quad (30)$$

end:

$$\eta \rightarrow \infty: \quad \frac{df}{d\eta}(\infty) \rightarrow 0, \quad h(\infty) \rightarrow 0, \quad j(\infty) \rightarrow 0, \quad g(\infty) \rightarrow 0. \quad (31)$$

The rate of heat transfer from the wall is given by:

$$q_w = -k_f \frac{\partial T}{\partial y} \Big|_{y=0} = -k_f (T_w - T_\infty) \left(\frac{a}{\nu} \right)^{1/2} h'(0), \quad (32)$$

where k_f is the coefficient of thermal conductivity and a is the stretching parameter. We can further define the dimensionless wall shear stress and wall couple stress functions, but these are omitted here for brevity.

4 Numerical solution by the finite element method

The finite element method is used to generate accurate, efficient solutions to the transformed two-point boundary value problem viz equations (26) to (29) with corresponding boundary conditions (30) and (31). Details of the method are available in Reddy [25] and Bathe [26]. We introduce the substitution:

$$\frac{df}{d\eta} = A, \quad (33)$$

where A is the dimensionless velocity.

The equations (26) to (29) are therefore reduced to the following, where $()'$ indicates $d/d\eta$:

$$A'' + B_1 g' + f A' + Gr_x Re_x h + Gm_x Re_x j - A^2 - \frac{1}{Da_x Re_x} A = 0, \quad (34)$$

$$\lambda g'' - \frac{\lambda}{G^*} (2g + A') - Ag + fg' = 0, \quad (35)$$

$$h'' + Pr f h' + Pr Ec A'^2 = 0, \quad (36)$$

$$j'' + Sc f j' - Sc Re_x \chi j = 0. \quad (37)$$

The corresponding boundary conditions are:

$$\eta = 0: \quad f(0) = 0, \quad A(0) = 1, \quad h(0) = 1, \quad j(0) = 1, \quad g(0) = -sA'(0), \quad (38)$$

$$\eta \rightarrow \infty: \quad A \rightarrow 0, \quad h \rightarrow 0, \quad j \rightarrow 0, \quad g \rightarrow 0. \quad (39)$$

Convergence has been efficiently achieved by fixing infinity as 8. The whole domain is discretized into a set of 70 line elements of equal width, each element being two-noded.

4.1 Variational formulation

The variational form associated with equations (33)–(37) over a typical two noded-linear element (η_e, η_{e+1}) is given by:

$$\int_{\eta_e}^{\eta_{e+1}} w_1 \{f' - A\} d\eta = 0, \quad (40)$$

$$\int_{\eta_e}^{\eta_{e+1}} w_2 \left\{ A'' + B_1 g' + f A' + Gr_x Re_x h + Gm_x Re_x j - A^2 - \frac{1}{Da_x Re_x} A \right\} d\eta = 0, \quad (41)$$

$$\int_{\eta_e}^{\eta_{e+1}} w_3 \left\{ \lambda g'' - \frac{\lambda}{G^*} (2g + A') - Ag + fg' \right\} d\eta = 0, \quad (42)$$

$$\int_{\eta_e}^{\eta_{e+1}} w_4 \{h'' + Pr f h' + Pr Ec A'^2\} d\eta = 0, \quad (43)$$

$$\int_{\eta_e}^{\eta_{e+1}} w_5 \{j'' + Sc f j' - Sc Re_x \chi j\} d\eta = 0, \quad (44)$$

where w_1, w_2, w_3, w_4 and w_5 are arbitrary test functions and may be viewed as the variation in f, A, h, j and g respectively.

4.2 Finite element formulation

The finite element method seeks an approximate solution to the differential equation over each element. The polynomial approximation of the solution within a two-noded element is of the form:

$$f = \sum_{j=1}^2 f_j \psi_j, \quad A = \sum_{j=1}^2 A_j \psi_j, \quad h = \sum_{j=1}^2 h_j \psi_j, \quad j = \sum_{j=1}^2 j_j \psi_j, \quad g = \sum_{j=1}^2 g_j \psi_j, \quad (45)$$

where f_j, A_j, h_j, j_j and g_j are the values of the solution at the j -th node of the element and ψ_i are the shape functions for a typical element (η_e, η_{e+1}) and are taken as:

$$\psi_1^{(e)} = \frac{\eta_{e+1} - \eta}{\eta_{e+1} - \eta_e}, \quad \psi_2^{(e)} = \frac{\eta - \eta_e}{\eta_{e+1} - \eta_e}, \quad \eta_e \leq \eta \leq \eta_{e+1}. \quad (46)$$

The coefficients f_j, A_j, h_j, j_j and g_j are determined such that the equation (40)–(44) are satisfied in the weighted integral sense.

Taking $w_1 = w_2 = w_3 = w_4 = w_5 = \psi_i$ ($i = 1, 2$), the finite element model of the equations thus formed is given by

$$\begin{bmatrix} [K^{11}] & [K^{12}] & [K^{13}] & [K^{14}] & [K^{15}] \\ [K^{21}] & [K^{22}] & [K^{23}] & [K^{24}] & [K^{25}] \\ [K^{31}] & [K^{32}] & [K^{33}] & [K^{34}] & [K^{35}] \\ [K^{41}] & [K^{42}] & [K^{43}] & [K^{44}] & [K^{45}] \\ [K^{51}] & [K^{52}] & [K^{53}] & [K^{54}] & [K^{55}] \end{bmatrix} \begin{bmatrix} \{f\} \\ \{A\} \\ \{h\} \\ \{j\} \\ \{g\} \end{bmatrix} = \begin{bmatrix} \{b^1\} \\ \{b^2\} \\ \{b^3\} \\ \{b^4\} \\ \{b^5\} \end{bmatrix}, \quad (47)$$

where $[K^{mn}]$ and $[b^m]$ ($m, n = 1, 2, 3, 4, 5$) are the matrices of order 2×2 and 2×1 respectively. We define some of the above matrices as follows:

$$K_{ij}^{11} = \int_{\eta_e}^{\eta_{e+1}} \psi_i \frac{d\psi_j}{d\eta} d\eta, \quad K_{ij}^{12} = - \int_{\eta_e}^{\eta_{e+1}} \psi_i \psi_j d\eta, \quad K_{ij}^{13} = K_{ij}^{14} = K_{ij}^{15} = 0, \quad (48)$$

$$K_{ij}^{21} = 0, \quad (49)$$

$$K_{ij}^{23} = Gr_x Re_x \int_{\eta_e}^{\eta_{e+1}} \psi_i \psi_j d\eta, \quad K_{ij}^{24} = Gm_x Re_x \int_{\eta_e}^{\eta_{e+1}} \psi_i \psi_j \eta, \quad (50)$$

$$K_{ij}^{25} = B_1 \int_{\eta_e}^{\eta_{e+1}} \psi_i \frac{d\psi_j}{d\eta} d\eta, \quad (51)$$

$$K_{ij}^{31} = 0, \quad K_{ij}^{32} = -\frac{\lambda}{G^*} \int_{\eta_e}^{\eta_{e+1}} \psi_i \frac{d\psi_j}{d\eta} d\eta, \quad (52)$$

$$\begin{aligned} K_{ij}^{35} = & -\lambda \int_{\eta_e}^{\eta_{e+1}} \frac{d\psi_i}{d\eta} \frac{d\psi_j}{d\eta} d\eta - \frac{2\lambda}{G^*} \int_{\eta_e}^{\eta_{e+1}} \psi_i \psi_j d\eta - \overline{A_1} \int_{\eta_e}^{\eta_{e+1}} \psi_i \psi_1 \psi_j d\eta \\ & - \overline{A_2} \int_{\eta_e}^{\eta_{e+1}} \psi_i \psi_2 \psi_j d\eta + \overline{f_1} \int_{\eta_e}^{\eta_{e+1}} \psi_i \psi_1 \frac{d\psi_i}{d\eta} d\eta + \overline{f_2} \int_{\eta_e}^{\eta_{e+1}} \psi_i \psi_2 \frac{d\psi_i}{d\eta} d\eta, \end{aligned} \quad (53)$$

$$K_{ij}^{41} = 0, \quad (54)$$

$$K_{ij}^{42} = Pr Ec \overline{A_1} \int_{\eta_e}^{\eta_{e+1}} \psi_i \frac{d\psi_1}{d\eta} \frac{d\psi_j}{d\eta} d\eta + Pr Ec \overline{A_2} \int_{\eta_e}^{\eta_{e+1}} \psi_i \frac{d\psi_2}{d\eta} \frac{d\psi_j}{d\eta} d\eta, \quad (55)$$

$$\begin{aligned} K_{ij}^{43} = & - \int_{\eta_e}^{\eta_{e+1}} \frac{d\psi_i}{d\eta} \frac{d\psi_j}{d\eta} d\eta + Pr \overline{f_1} \int_{\eta_e}^{\eta_{e+1}} \psi_i \psi_1 \frac{d\psi_j}{d\eta} d\eta, \\ & + Pr \overline{f_2} \int_{\eta_e}^{\eta_{e+1}} \psi_i \psi_2 \frac{d\psi_j}{d\eta} d\eta, \end{aligned} \quad (56)$$

$$K_{ij}^{44} = K_{ij}^{45} = 0, \quad (57)$$

$$K_{ij}^{51} = K_{ij}^{52} = K_{ij}^{53} = 0, \quad (58)$$

$$\begin{aligned} K_{ij}^{54} = & - \int_{\eta_e}^{\eta_{e+1}} \frac{d\psi_i}{d\eta} \frac{d\psi_j}{d\eta} d\eta + Sc \overline{f_1} \int_{\eta_e}^{\eta_{e+1}} \psi_i \psi_1 \frac{d\psi_j}{d\eta} d\eta \\ & + Sc \overline{f_2} \int_{\eta_e}^{\eta_{e+1}} \psi_i \psi_2 \frac{d\psi_j}{d\eta} d\eta - Sc Re_x \chi \int_{\eta_e}^{\eta_{e+1}} \psi_i \psi_j d\eta, \end{aligned} \quad (59)$$

$$K_{ij}^{55} = 0, \quad (60)$$

$$b_i^1 = 0, \quad b_i^2 = -\left(\psi_i \frac{dA}{d\eta}\right)_{\eta_e}^{\eta_{e+1}}, \quad b_i^3 = -\lambda \left(\psi_i \frac{dg}{d\eta}\right)_{\eta_e}^{\eta_{e+1}}, \quad (61)$$

$$b_i^4 = -\left(\psi_i \frac{dh}{d\eta}\right)_{\eta_e}^{\eta_{e+1}}, \quad b_i^5 = -\left(\psi_i \frac{dj}{d\eta}\right)_{\eta_e}^{\eta_{e+1}},$$

where

$$\overline{f} = \sum_{i=1}^2 \overline{f_i} \psi_i, \quad \overline{A} = \sum_{i=1}^2 \overline{A_i} \psi_i. \quad (62)$$

Each element matrix is of the order 10×10 . Since the whole domain is divided into a set of 70 line elements, following assembly of all the element equations we obtain a matrix of order 355×355 . This system is non-linear and hence dealing with it is facilitated by a linearization procedure. The system is linearized by incorporating the functions \bar{f} and \bar{A} , which are assumed to be known. After this the linearized system is solved iteratively. Applying the given boundary conditions only a system of 346 equations remains to be solved. At the beginning of the first iteration the velocity, temperature, concentration and microrotation are taken to be zero and the system of equations is solved using a Gaussian elimination method for the nodal velocity, temperature, concentration and microrotation. Thus the values at the first iteration are obtained. This process is repeated until the desired accuracy of 0.0005 is obtained.

5 Results and discussion

In the present study we have adopted the following default parameter values for the finite element computations: $Gr_x = 1.0$, $Gm_x = 1.0$, $\chi = 1.0$, $Da_x = 1.0$, $Re_x = 1.0$, $Pr = 0.7$, $Sc = 0.1$, $B_1 = 0.01$, $G^* = 1$, $\lambda = 1$, $s = 0.5$ and $Ec = 0.02$. *These values are used throughout the computations, unless otherwise indicated.* Comparisons have also been made with the finite difference method (details are not provided here for brevity) and results are shown in Table 1. Excellent correlation is observed between both methods for the special case of $Da_x = 1.0$, for dimensionless translational velocity profile (A) and also for dimensionless micro-rotation (g) profile.

Table 1. Comparison table of finite difference and finite element computations

$s = 0.5, Sc = 0.1, Pr = 0.7, Re_x = 1, Gr_x = 1, Gm_x = 1,$ $B_1 = 0.01, G^* = 1, \lambda = 1, Ec = 0.02, \chi = 1$				
η	$A (Da = 1.0)$		$g (Da = 1.0)$	
	FEM	FDM	FEM	FDM
0	1	1	0.07887	0.07886
0.914286	0.743958	0.743956	0.114158	0.114157
1.94286	0.415178	0.415177	0.087409	0.087409
2.97143	0.217921	0.217920	0.048231	0.048231
4	0.115855	0.115855	0.025734	0.025734
5.02857	0.060083	0.060082	0.014358	0.014358
6.05714	0.027294	0.027292	0.007764	0.007763
7.08571	0.008198	0.008195	0.003153	0.003151
8	0	0	0	0

Fig. 2 illustrates the influence of the **micropolar coupling constant** B_1 on the velocity and micro-rotation (angular velocity) profiles. We note that $B_1 = 0$ implies Newtonian flow and the vanishing of micropolarity. Equation (26) for this case reduces

to:

$$\frac{d^3 f}{d\eta^3} + f \frac{d^2 f}{d\eta^2} - \left(\frac{df}{d\eta}\right)^2 + Gr_x Re_x h + Gm_x Re_x j - \frac{1}{Re_x Da_x} \frac{df}{d\eta} = 0.$$

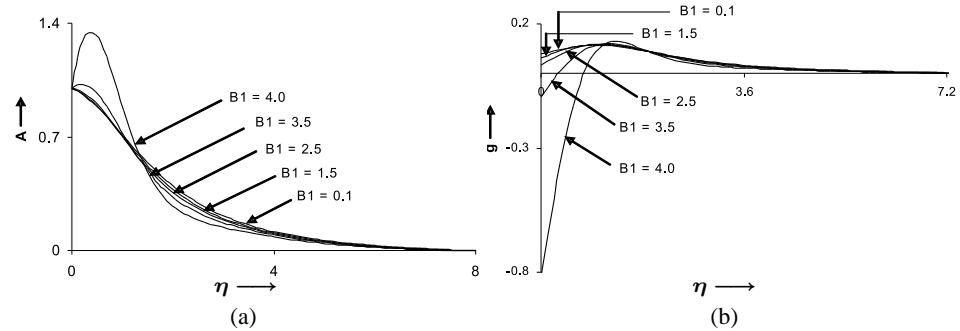


Fig. 2. (a) A versus η for various B_1 values; (b) g versus η for various B_1 values. $s = 0.5$, $Sc = 0.1$, $Pr = 0.7$, $Re_x = 1$, $Da_x = 1$, $Gm_x = 1$, $Gr_x = 1$, $G^* = 1$, $\lambda = 1$, $Ec = 0.02$, $\chi = 1$.

The micro-rotation equation (27) also disappears. For low values of B_1 i.e. 0.1, there is weak micropolar vortex viscosity. We observe that translational velocity (A) increases markedly with B_1 values as the latter increase from 0.1 to 4.0 (strong vortex viscosity). A peak velocity of 1.3 occurs for $B_1 = 4$ at approximately $\eta = 0.5$ i.e. very close to the wall. This trend is maintained until $\eta \sim 1.5$ at which stage A values are depressed by an increase in micropolar coupling constant. For the remainder of the domain velocity is increased marginally with a rise in B_1 values; all profiles converge asymptotically to zero, far from the wall. Strongly micropolar fluid is therefore *accelerated* in the near-wall regime whereas it is decelerated in the far-field regime. Fig. 2(b) indicates that magnitudes of micro-rotation, g , are increased with higher values of the coupling parameter, B_1 . For lower values of B_1 we observe that micro-rotation is actually reversed. The lowest magnitude of g corresponds to $B_1 = 0.1$ and is approximately 0.1; the peak magnitude for $B_1 = 4.0$ however is 0.8 and occurs (as with all other profiles) at the wall i.e. $\eta = 0$. All micro-rotation profiles have non-zero value at the wall and at $\eta \sim 1$ they intersect and decay smoothly to zero at the end of the regime. The graphs in Fig. 2 corresponds to *weakly buoyant Darcian flow with low viscous dissipation*, the parameters having default values, discussed earlier.

The influence of the **Eckert number** i.e. viscous dissipation parameter (Ec) on translational velocity, angular velocity and dimensionless temperature profiles is illustrated in Fig. 3. Ec expresses the relationship between the kinetic energy in the flow and the enthalpy [24]. It embodies the conversion of *kinetic energy* into *internal energy* by work done against the viscous fluid stresses. Although this parameter is often used in high-speed compressible flow, for example in rocket aerodynamics at very high altitude, it has significance in high temperature incompressible flows, which are encountered in

chemical engineering systems, radioactive waste repositories, nuclear engineering systems etc. Positive Eckert number implies cooling of the wall and therefore a transfer of heat to the fluid. Convection is enhanced and we observe in consistency with for example Schlichting [24], Soundalgekar and Takhar [19], Mansour and Gorla [20] etc. that the fluid is accelerated i.e. translational velocity is increased in the micropolar fluid. Temperatures are also boosted as shown in Fig. 3(b) since internal energy is increased. Micro-rotation however is *reduced* by a rise in Ec values from 0.02 through 1, 2, 3 to 4, in the vicinity of the wall. Hence the *minimum* value of micro-rotation at the wall corresponds to $Ec = 4$, and this value is 0.02 approximately. As Ec values decrease, dissipation effects fall and the micro-rotation consistently increases over the near wall regime, $0 < \eta < 1.5$ approximately. At $\eta = 1.5$ all profiles converge and the reverse effect is observed on micro-rotation, g , for the remainder of the domain. Hence for $1.5 < \eta < 8$, we see that a rise in Ec induces a slight increase in the g values. All profiles descend smoothly to zero at the end of the range i.e. in the free stream.

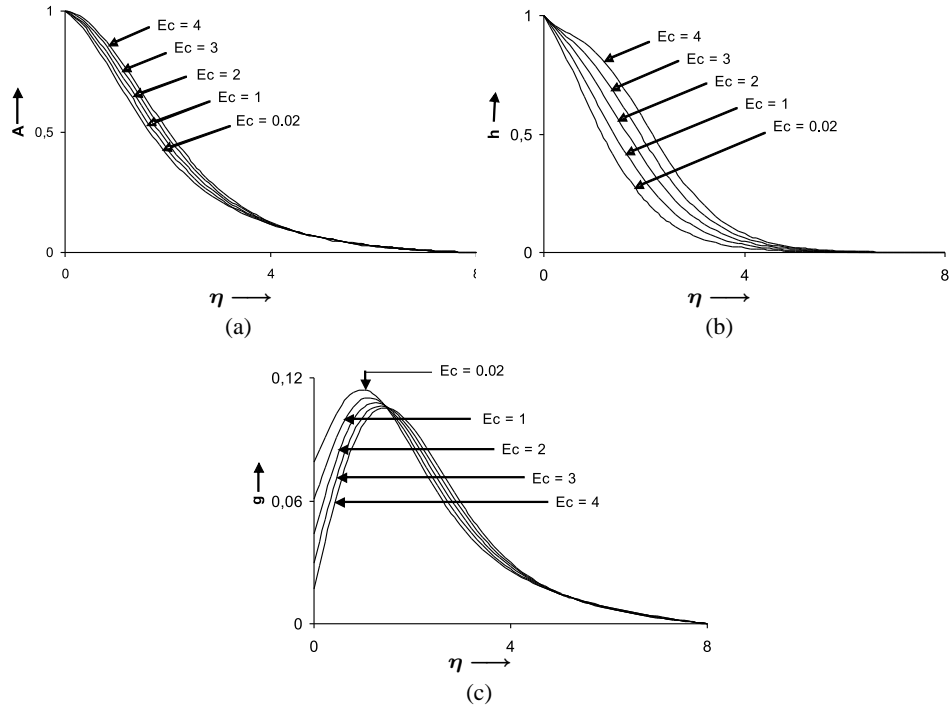


Fig. 3. (a) A versus η for various Ec values; (b) h versus η for various Ec values; g versus η for various Ec values. $s = 0.5$, $Sc = 0.1$, $Pr = 0.7$, $Re_x = 1$, $Da_x = 1$, $Gm_x = 1$, $Gr_x = 1$, $G^* = 1$, $\lambda = 1$, $B_1 = 0.01$, $\chi = 1$.

The effects of the **Prandtl number** on velocity, temperature and micro-rotation profiles are depicted in Fig. 4. Pr encapsulates the ratio of momentum diffusivity to thermal

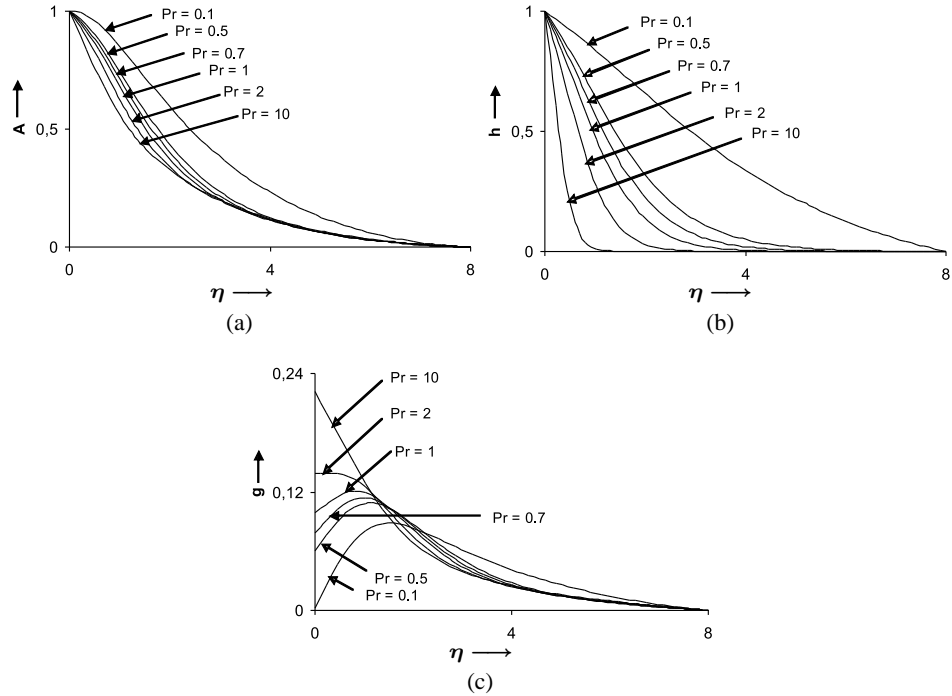


Fig. 4. (a) A versus η for various Pr values; (b) h versus η for various Pr values; g versus Pr for various Ec values. $s = 0.5$, $Sc = 0.1$, $Ec = 0.02$, $Re_x = 1$, $Da_x = 1$, $Gm_x = 1$, $Gr_x = 1$, $G^* = 1$, $\lambda = 1$, $B_1 = 0.01$, $\chi = 1$.

diffusivity. Larger Pr values imply a thinner thermal boundary layer thickness and more uniform temperature distributions across the boundary layer. Hence the thermal boundary layer will be much less in thickness than the hydrodynamic (translational velocity) boundary layer. $Pr = 1$ implies that the thermal and velocity boundary layers are approximately equal in extent [24]. Smaller Pr fluids have higher thermal conductivities so that heat can diffuse away from the vertical surface faster than for higher Pr fluids (thicker boundary layers). Physically the lower values of Pr correspond to liquid metals ($Pr \sim 0.02, 0.05$), $Pr = 0.7$ is accurate for air or hydrogen and $Pr = 1$ for water. The computations show that translational velocity, A , (Fig. 4(a)) is therefore reduced as Pr rises from 0.1, through 0.5, 0.7 to 1.0, 2.0 and 10.0 since the fluid is increasingly viscous as Pr rises. Hence the micropolar fluid is decelerated with a rise in Pr . Fig. 4(b) indicates that a rise in Pr substantially reduces the temperature, h , in the micropolar-fluid-saturated porous regime. Our computations correlate well with the earlier study on coupled micropolar heat and mass transfer in porous media by Kim [11]. The profiles become increasingly parabolic as Pr increases above 0.1, for which the profile is approximately a linear decay. For all cases, h decays to zero as $\eta \rightarrow \infty$, i.e. in the freestream. There is however a rapid decay to zero for the maximum Pr ($= 10$) where the temperature plummets to zero in

the near-wall region. The influence of Pr on micro-rotation, g , however is positive; g values increase both at and near the wall, as Pr increases from 0.1 to 10. Maximum micro-rotation is observed for $Pr = 10$ and has a value of 0.22. With lower values of Pr (0.2, 0.5, 0.7, 1) the profiles all rise from the wall to $\eta \sim 1$; for $Pr = 2, 10$ however they descend from the wall. In all cases profiles decay smoothly to zero as $\eta \rightarrow \infty$.

Fig. 5 illustrates the profiles of translational velocity and micro-rotation versus η for various **local Darcy numbers**, Da_x . This parameter simulates the effects of the bulk matrix impedance due to the porous medium fibers. Fig. 5(a) indicates that a rise in Da_x (which implies a rise in permeability, k_p) enhances considerably the translational velocity of the micropolar fluid (Fig. 5(a)). Hence the micropolar fluid is accelerated with a rise in Da_x . With increasing permeability the porous matrix structure becomes less and less prominent and in the limit of infinite Da_x values, the porous medium vanishes. Equation (26) shows that the Darcian body force is inversely proportional to Da_x . Therefore higher Da_x values will reduce the porous bulk retarding force. These numerical computations also indicate that the presence of a porous medium with low permeability (high solid material presence) may be implemented successfully as a mechanism for controlling flow velocities in chemical engineering applications since lower permeability media induce a deceleration in transport. Micro-rotation values (Fig. 5(b)) however are substantially decreased as Da_x increases from 0.1 (low permeability) through 1, 2, 5 and to 20 (high permeability) for the near-wall regime; however for $\eta > 2$ i.e. a quarter-distance along the domain from the wall, increasing local Da_x enhances the micro-rotation values. We may infer that close to the wall, micro-rotation is inhibited even for more permeable media as the particles have difficulty in rotating due to the presence of the wall; however further from the wall, with a more permeable environment, the micropolar spin is less inhibited and microelements can rotate more freely, as demonstrated by the slightly larger values of g for $Da_x = 20$ compared with lower Da_x values for the regime $2 < \eta < 8$.

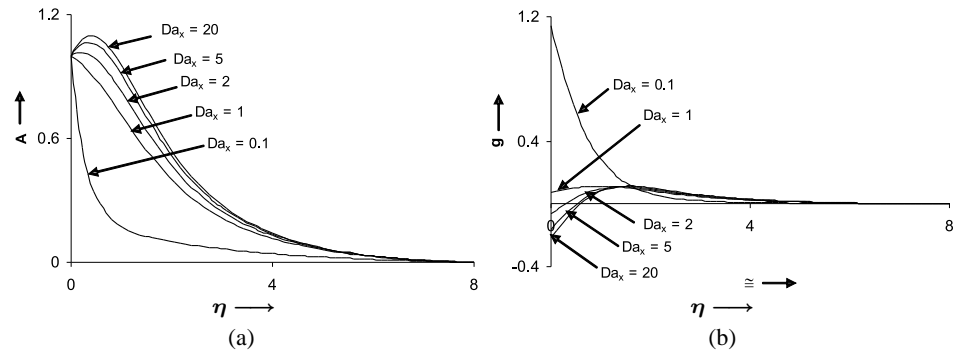


Fig. 5. (a) A versus η for various Da_x values; (b) g versus η for various Da_x values. $s = 0.5$, $Sc = 0.1$, $Pr = 0.7$, $Re_x = 1$, $Gm_x = 1$, $Gr_x = 1$, $B_1 = 0.01$, $G^* = 1$, $\lambda = 1$, $Ec = 0.02$, $\chi = 1$.

Fig. 6 shows the influence of **surface parameter**, s , on the flow regime. Micro-

rotation is seen to increase substantially over the range $0 < \eta < 1.5$, as s increases from 0 to 1.0. $s = 0$ implies that micro-rotation at the wall is prevented so that micro-rotation vanishes at the wall for this case. Increasing s raises the degree of intensity of microelement rotation generating the peak angular velocity of 0.16 for $s = 1.0$. At approximately $\eta = 1.5$ all profiles merge and owing to the distance from the wall, the surface parameter, s , no longer exerts an effect on micro-rotation field. Therefore all profiles are superimposed and descend to zero smoothly in the free stream.

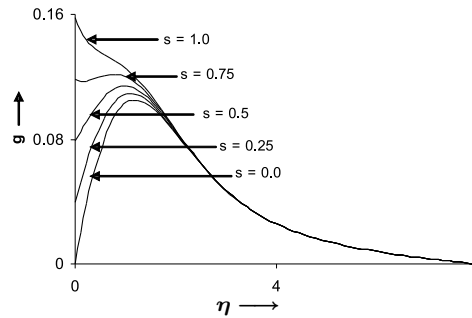


Fig. 6. g versus η for various s values. $Sc = 0.1$, $Pr = 0.7$, $Re_x = 1$, $Da_x = 1$, $Gm_x = 1$, $Gr_x = 1$, $B_1 = 0.01$, $G^* = 1$, $\lambda = 1$, $Ec = 0.02$, $\chi = 1$.

Fig. 7 shows the effect of the **Schmidt number**, Sc , on the dimensionless concentration (j) and the gradient of the dimensionless concentration (j'). We note that Sc i.e. the Schmidt number, embodies the ratio of the momentum to the mass diffusivity. Sc therefore quantifies the relative effectiveness of momentum and mass transport by diffusion in the hydrodynamic (velocity) and concentration (species) boundary layers. Smaller Sc values can represent for example hydrogen gas as the species diffusing ($Sc = 0.1$ to 0.2). $Sc = 1.0$ corresponds approximately to carbon dioxide diffusing in air, $Sc = 2.0$ implies hydrocarbon diffusing in air, and higher values to petroleum derivatives diffusing in fluids (e.g. ethylbenzene) as indicated by Gebhart et al. [27]. We have presented the computations for $Pr = 0.7$. In all profiles of j versus η , for various Sc values, $Pr \neq Sc$. The thermal and species diffusion regions are of different extents. As Sc increases, Fig. 7(a) shows that j values are strongly decreased, as larger values of Sc correspond to a decrease in the chemical molecular diffusivity i.e. less diffusion therefore takes place by *mass* transport. The dimensionless concentration profiles all decay from a maximum concentration of 1 at $\eta = 0$ (the wall boundary condition) to zero in the freestream. A very steep decay is witnessed in j values for high Sc , and these profiles descend quickly to zero before $\eta = 1$. Species transfer is therefore considerably inhibited only a short distance from the stretching surface for high Sc values (5, 10), whereas for lower Sc values (0.1, 0.5, 1, 2) a more gentle fall is observed; j values generally reach zero quite far from the wall in these latter cases. Dimensionless concentration gradient (j') is also seen in Fig. 7(b) to fall with a rise in Schmidt number, in particular in the vicinity of the wall.

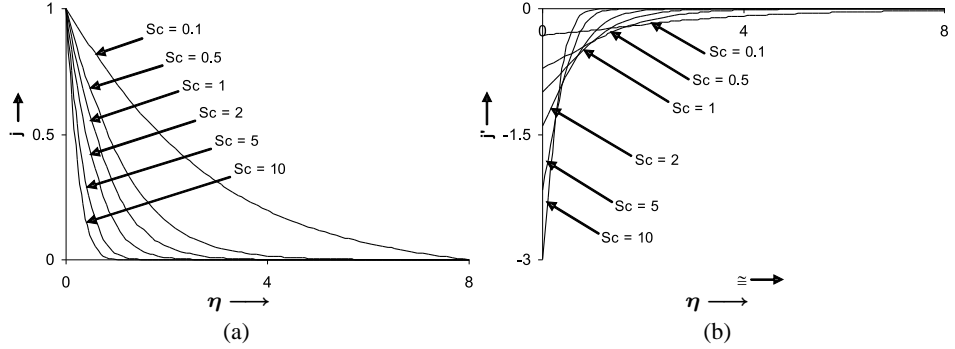


Fig. 7. (a) j versus η for various Sc values; (b) j' versus η for various Sc values. $s = 0.5, Pr = 0.7, Re_x = 1, Da_x = 1, Gm_x = 1, Gr_x = 1, B_1 = 0.01, G^* = 1, \lambda = 1, Ec = 0.02, \chi = 1.$

The influence of **local Reynolds number**, Re_x , on A and g is shown in Fig. 8. As Re_x increases, the flow momentum increases and as expected the translational velocity (Fig. 8(a)) increases considerably. The flow however is still Darcian as the Darcy model is valid up to $Re_x \sim 10$, as described by Bear [28]. The regime is still weakly buoyant with dissipation and chemical reaction present. At very low Reynolds numbers, a sharp decay from the wall value of unity (initial boundary condition) to very low values is observed. For $Re_x = 0.5, 1, 1.5$ and 2 , the profiles descend more gradually to zero from unity value at the wall. Micro-rotation profiles are seen to be depressed by an increase in local Reynolds number. The peak value of g therefore occurs for $Re_x = 0.1$ (at the wall), and the minimum value is -0.5 for $Re_x = 2$, again at the wall. All the g profiles converge at approximately $\eta = 1.5$ and after this micro-rotation is slightly increased by larger Reynolds numbers. The distributions all decay to zero thereafter.

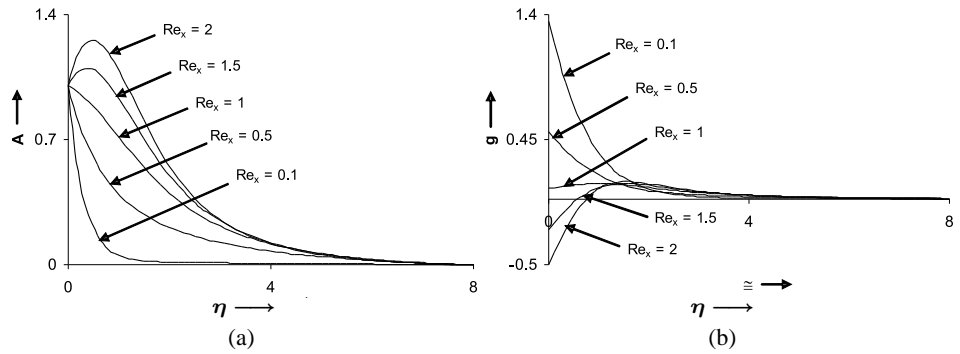


Fig. 8. (a) A versus η for various Re_x values; (b) g versus η for various Re_x values. $s = 0.5, Sc = 0.1, Pr = 0.7, Da_x = 1, Gm_x = 1, Gr_x = 1, B_1 = 0.01, G^* = 1, \lambda = 1, Ec = 0.02, \chi = 1.$

The variation of translational velocity, temperature function, concentration function and micro-rotation function with η , for various values of the **chemical reaction number** (χ) are depicted in Fig. 9. An increase in the χ value induces a marked decrease in the translational velocity (Fig. 9(a)), A , throughout the entire regime. In all cases, the profiles decay from unity at the vertical stretching surface wall ($\eta = 0$), gradually to zero at the freestream ($\eta \rightarrow \infty$). Chemical reaction rate clearly decelerates the flow of the micropolar fluid. We note that the parameter values for B_1, G^* and Ec also imply a weakly micropolar flow scenario with weak mechanical dissipation effects. Chemical reaction stifles diffusive transport and thereby retards the flow momentum. As a result *maximum* translational velocity occurs for the case of zero chemical reaction i.e. $\chi = 0$. Fig. 9(b) shows that temperature function profiles i.e. h values are elevated with a rise in chemical reaction parameter. The profiles are not as widely dispersed as for the translational velocity distributions; there is nevertheless a distinct rise in temperatures, in particular at the location $\eta \sim 3$. The present computations concur well with earlier studies of free convection with chemical reaction, such as those presented recently by Afify [29]. Temperature profiles are seen to be minimized in the absence of chemical

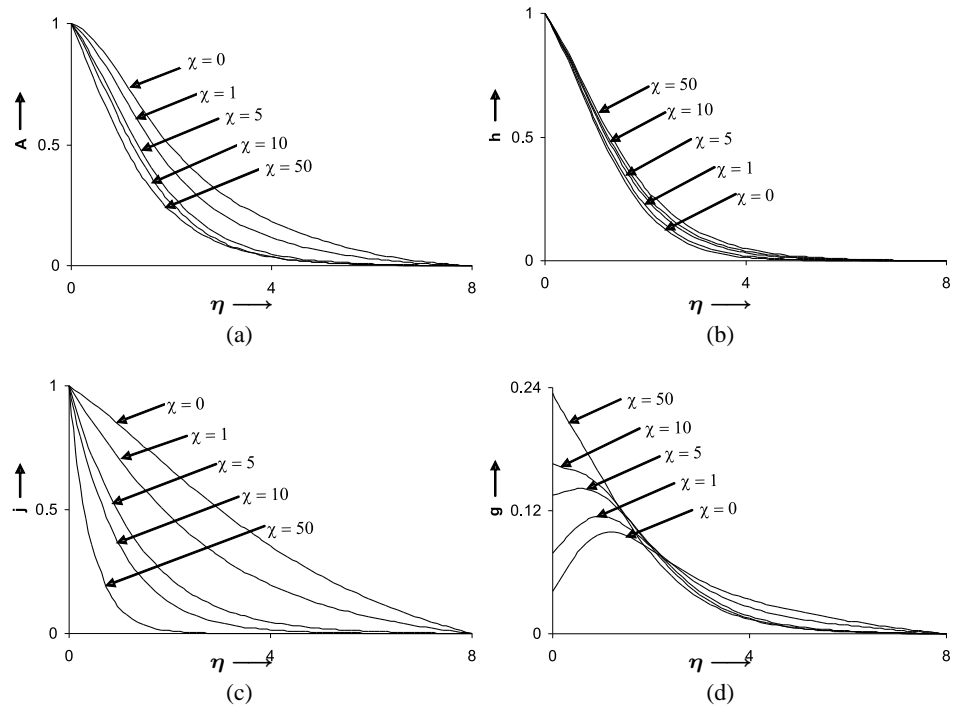


Fig. 9. (a) A versus η for various χ values; (b) h versus η for various χ values; (c) j versus η for various χ values; (d) g versus η for various χ values. $s = 0.5$, $Sc = 0.1$, $Pr = 0.7$, $Re_x = 1$, $Da_x = 1$, $Gm_x = 1$, $Gr_x = 1$, $B_1 = 0.01$, $G^* = 1$, $\lambda = 1$, $Ec = 0.02$.

reaction. The effect of χ on the dimensionless concentration (j) distributions is illustrated in Fig. 9(c), wherein it is clear that as χ rises from 0 to 1, 5, 10 and 50 the j values are strongly reduced. As χ is increased the profiles become more monotonic in nature; in particular the gradient of the profile becomes much steeper for χ values equal to or greater than 5 compared with lower values of the chemical reaction parameter. Chemical reaction parameter therefore reduces magnitude of the dimensionless concentration, j , but increases the rate of change of species (mass) transfer function, since higher χ values imply a *faster* rate of reaction. Fig. 9(d) shows that micro-rotation (g) is noticeably boosted at the wall with a rise in reaction parameter. This trend is sustained up to $\eta \sim 1.8$ after which micro-rotation is depressed by a rise in χ . Our results agree generically with those presented by Seddeek [30].

Finally the effects of **thermal and species Grashof number** i.e. Gr_x and Gm_x are shown in Figs. 10, 11, for the velocity, temperature and species transfer distributions. Fig. 10(a) indicates that an increase in Gr_x from 1 through 2, 3, 5, to 10 strongly boosts the translational velocity in particular over the zone $0 < \eta < 2$. There is a rapid rise in the A value near the stretching surface (wall) especially for the cases $Gr_x = 5$ and 10. Peak velocity for $Gr_x = 10$ is about 1.8 occurring at $\eta \sim 0.5$. At $\eta \sim 2$ there is a switch in the effect of the thermal Grashof number by increasing from 1 to 10 is now seen to reduce the translational velocity. The profiles generally descend smoothly towards zero although the rate of descent is greater corresponding to higher thermal Grashof numbers. Gr_x defines the ratio of the thermal buoyancy force to the viscous hydrodynamic force and as expected does accelerate the flow. Temperature distribution h versus η is plotted in Fig. 10(b) and is seen to decrease with a rise in thermal Grashof number, a result which agrees with fundamental studies on free convection [24]. This decrease is most pronounced at $\eta \sim 2$.

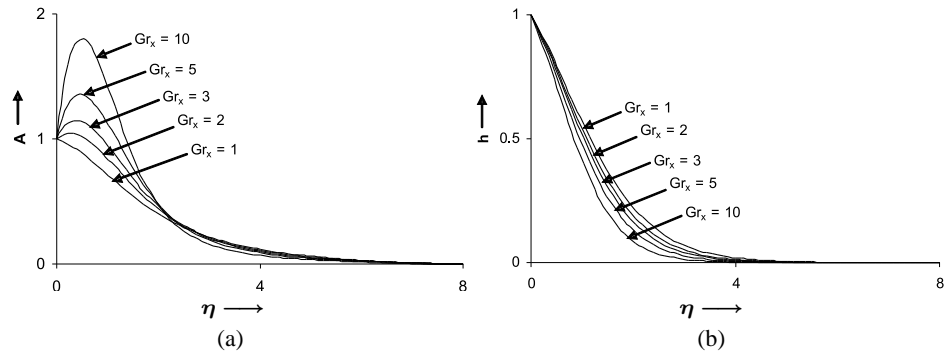


Fig. 10. (a) A versus η for various Gr_x values; (b) h versus η for various Gr_x values. $s = 0.5$, $Sc = 0.1$, $Pr = 0.7$, $Re_x = 1$, $Da_x = 1$, $Gm_x = 1$, $B_1 = 0.01$, $G^* = 1$, $\lambda = 1$, $Ec = 0.02$, $\chi = 1$.

The effects of the **species Grashof number** on translational velocity, temperature function, concentration function and micro-rotation are presented in Fig. 11. Translational

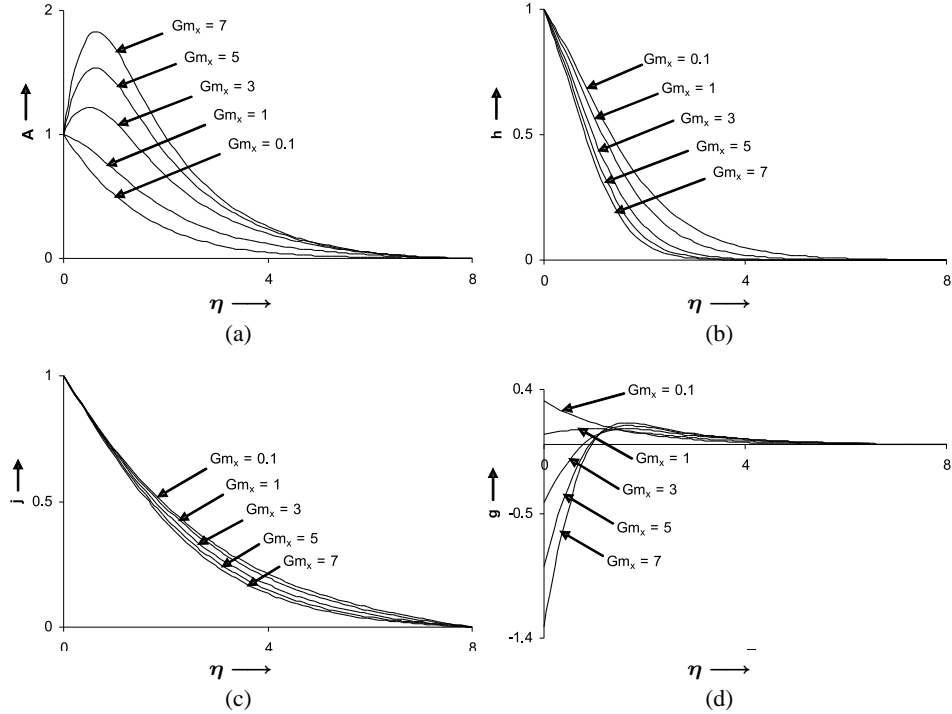


Fig. 11. (a) A versus η for various Gm_x values; (b) h versus η for various Gm_x values; (c) j versus η for various Gm_x values; (d) g versus η for various Gm_x values. $s = 0.5$, $Sc = 0.1$, $Pr = 0.7$, $Re_x = 1$, $Da_x = 1$, $Gr_x = 1$, $B_1 = 0.01$, $G^* = 1$, $\lambda = 1$, $Ec = 0.02$, $\chi = 1$.

velocity, A , is observed to increase considerably with a rise in Gm_x from 0.1 to 7. Hence species Grashof number boosts velocity of the micropolar fluid indicating that buoyancy has an accelerating effect on the flow field. Temperature, h , undergoes a marked decrease in value however with a rise in species Grashof number, as illustrated in Fig. 11(b). All temperatures descend from unity at the wall to zero at the freestream. The depression in temperatures is maximized by larger species Grashof numbers in the vicinity $\eta \sim 2$, indicating a similar trend to the influence of the thermal Grashof number (Fig. 10(b)). Dimensionless concentration, j , as depicted in Fig. 11(c), is also seen to be reduced by increasing the species Grashof number. All profiles decay smoothly from unity at the vertical stretching surface to zero as $\eta \rightarrow \infty$. Hence mass transfer buoyancy has a regulatory effect on the species (dimensionless concentration) field and such a trend can be exploited in chemical reactor design. With regard to environmental contamination flows, our results would indicate that buoyancy depresses the magnitudes of concentration of contaminant in a porous regime e.g. geomaterial. Finally the influence of Gm_x on micro-rotation profiles is shown in Fig. 11(d). The micro-rotation component g is

considerably reduced with a rise in Gm_x values at the wall. For $Gm_x = 0.1$ the peak value at the wall is 0.35; this decreases to -1.3 for $Gm_x = 7$. At $\eta \sim 1$, the trend is reversed and we observe that mass Grashof number now marginally boosts the micro-rotation values. For all Gm_x values the profiles remain positive for $\eta > 2$ and decay gradually to zero at the freestream.

6 Conclusions

Numerical solutions have been presented for the two-dimensional chemically-reactive, dissipative free convective heat and mass transfer in an incompressible micropolar-fluid-saturated Darcian porous medium adjacent to a vertical stretching surface. The results indicate that:

1. Increasing the micropolar coupling parameter (ratio of the vortex and Newtonian viscosities) induce a rise in translational velocity near the wall and increases micro-rotation magnitudes near the wall.
2. Increasing the Eckert number (viscous heating parameter) increases both the translational velocity and temperature function throughout the regime; micro-rotation is however decreased in the near-wall zone with a rise in Eckert number but increased with Eckert number rising further from the vertical stretching surface.
3. Increasing the Prandtl number substantially decreases the translational velocity and the temperature function. Micro-rotation is however increased at the wall with a rise in Prandtl number but reduced further from the wall as we approach the free stream.
4. Increasing local Darcy number, Da_x , accelerates the flow i.e. increases translational velocities. However micro-rotation at the wall is reduced with a rise in local Darcy number. Further from the wall however a rise in local Darcy number (i.e. increasing permeability of the porous medium) increases slightly the values of micro-rotation.
5. Increasing the surface parameter substantially increases micro-rotation, g , particularly at and near the wall.
6. Increasing Schmidt number generally decreases the concentration j and also concentration gradient, j' , in particular near the wall.
7. Increasing the local Reynolds number, Re_x , strongly accelerates the flow i.e. increases translational velocity; micro-rotation is however decreased in particular at and near the stretching surface.
8. Increasing chemical reaction parameter decelerates the flow i.e. decreases translational velocity, increases temperature, decreases concentration, and boosts the micro-rotation at and in the vicinity of the wall.
9. Increasing thermal Grashof number, Gr_x , boosts the translational velocity in the near-wall regime and decreases temperature throughout the flow regime.

10. Increasing the species Grashof number, Gm_x , substantially increases the translational velocity throughout the micropolar fluid-saturated domain, depresses temperature function throughout the regime, decreases dimensionless concentration and also decreases micro-rotation values at the wall and in the near-wall regime.
11. The parameter value variation in practical flows does not differ significantly from those utilized in the graphs and as such our computations provide a good description of the effects of the thermophysical parameters on the heat, mass and momentum transfer in the regime.

Acknowledgement

The author (S. Rawat) acknowledges and is grateful for the financial assistanceship given to him by UGC (Univ. Grant Commission), INDIA. All the authors are grateful to the referees for their comments on this paper which helped to increase the quality of the work.

References

1. A. C. Eringen, Theory of Micropolar Fluids, *J. Math. and Mech.*, **16**, pp. 1–18, 1966.
2. A. C. Eringen, Simple microfluids, *Int. J. Engineering Science*, **2**, pp. 200–207, 1964.
3. R. Bhargava, L. Kumar, H. S. Takhar, Finite element solution of mixed convection micropolar flow driven by a porous stretching sheet, *Int. J. Engineering Science*, **41**, pp. 2161–2178, 2003.
4. A. J. Chamkha, T. Grosan, I. Pop, Fully Developed Combined Convection of a Micropolar Fluid in a Vertical Channel, *Int. J. Fluid Mechanics Research*, **30**, pp. 251–263, 2003.
5. M. Kaviany, *Principles of Heat Transfer in Porous Media*, MacGraw-Hill, New York, 1993.
6. A. J. Chamkha, Transient Power-Law Fluid Flow in a Porous Medium Channel, *Fluid/Particle Separation Journal*, **7**(1), pp. 4–7, 1994.
7. O. A. Bég, H. S. Takhar, T. A. Bég, A. J. Chamkha, G. Nath, R. Majeed, Modelling Convection Heat Transfer in a Rotating Fluid in a Thermally-Stratified High-Porosity Medium: Numerical Finite Difference Solutions, *Int. J. Fluid Mechanics Research*, **32**, pp. 383–401, 2005.
8. I. Aganovic, Z. Tutek, Homogenization of micropolar fluid flow through a porous medium, in: *Mathematical Modeling of Flow through Porous Media*, A. Bourgeat et al. (Eds.), World Scientific, pp. 2–13, 1995.
9. A. Mohammeadin, M. A. El-Hakim, S. M. El-Kabeir, M. A. Mansour, Natural convective flow of micropolar fluids in a porous medium, *Int. J. Applied Mechanics and Engineering*, **2**(2), pp. 187–204, 1997.
10. E. M. E. Elbarbary, N. S. Elgazery, Chebyshev finite difference method for the effects of radiation and variable viscosity on magneto-micropolar fluid flow through a porous medium, *Int. Comm. Heat and Mass Transfer*, **31**(3), pp. 409–419, 2004.
11. Y. J. Kim, Heat and mass transfer in MHD micropolar flow over a vertical moving porous plate in a porous medium, *Transp. Porous Media J.*, **56**, pp. 17–37, 2004.

12. A. J. Chamkha, A. Al-Mudhaf, J. Al-Yatama, Double-Diffusive Convective Flow of a Micropolar Fluid over a Vertical Plate Embedded in a Porous Medium with a Chemical Reaction, *Int. J. Fluid Mechanics Research*, **31**, pp. 529–551, 2004.
13. R. Bhargava, P. Bhargava, O. A. Bég, T. A. Bég, H. S. Takhar, Micropolar double-diffusive convection heat and mass transfer in a porous enclosure with heat source, *Meccanica J.*, submitted, June, 2006.
14. R. Rajasekaran, M. G. Palekar, Comparative effect of viscous dissipation on heat transfer in mixed convection flow: UWT and UHF cases, *Astrophysics Space Science J.*, **106**, pp. 73–80, 1984.
15. R. L. Mahajan, B. B. Gebhart, Viscous dissipation effects in buoyancy-induced flows, *Int. J. Heat Mass Transfer*, **32**(7), pp. 1380–1382, 1989.
16. O. A. Bég, V. Prasad, H. S. Takhar, V. M. Soundalgekar, Thermal convective flow in an isotropic, homogenous medium using Brinkman's vorticity diffusion model: Numerical Study, *Int. J. Numerical Methods in Heat and Fluid Flow*, **8**, pp. 59–89, 1998.
17. J. Koo, C. Kleinstreuer, Viscous dissipation effect in microtubes and microchannels, *Int. J. Heat Mass Transfer*, **47**, pp. 3156–2169, 2001.
18. O. Haddad, M. Abuzaid, M. Al-Nimr, Entropy generation due to laminar incompressible forced convection flow through parallel-plates microchannel, *Entropy J.*, **6**(5), pp. 413–426, 2004.
19. V. M. Soundalgekar, H. S. Takhar, Heat transfer in wedge flow of a micropolar fluid, in: *Proc. 8th Int. Conf. Rheology, Naples, Italy*, pp. 321–325, 1980.
20. M. A. Mansour, R. S. R. Gorla, Joule heating effects on unsteady natural convection from a heated vertical plate in a micropolar fluid, *Can. J. Physics*, **76**(12), pp. 977–984, 1998.
21. R. Bhargava, H. S. Takhar, Numerical study of heat transfer characteristics of micropolar boundary layer near a stagnation point on a moving wall, *Int. J. Engineering Science*, **38**, pp. 383–394, 2000.
22. A. C. Eringen, *Micro-continuum Field Theories II: Fluent Media*, Springer-Verlag, New York, 2001.
23. G. Lukaszewicz, *Micropolar Fluids: Theory and Applications*, Birkhauser, Boston, USA, 1999.
24. H. Schlichting, *Boundary-Layer Theory*, MacGraw-Hill, New York, 7th edition, 1979.
25. J. N. Reddy, *An Introduction to the Finite Element Method*, MacGraw-Hill, New York, 1985.
26. K. J. Bathe, *Finite Element Procedures*, Prentice-Hall, New Jersey, 1996.
27. B. Gebhart, Y. Jaluria, R. L. Mahajan, B. Sammakia, *Buoyancy-Induced Flows and Transport*, Hemisphere, New York, 1988.
28. J. Bear, *Dynamics of Fluids in Porous Media*, Dover, New York, 1972.
29. A. A. Afify, MHD free convective flow and mass transfer over a stretching sheet with chemical reaction, *Heat and Mass Transfer J.*, **40**(6–7), pp. 495–500, 2004.
30. M. A. Seddeek, Finite element method for the effects of chemical reaction, variable viscosity, thermophoresis, and heat generation/absorption on a boundary layer hydromagnetic flow with heat and mass transfer over a heated surface, *Acta Mechanica*, **40**, pp. 10–28, 2005.